Journal of Quantitative Spectroscopy & Radiative Transfer 302 (2023) 108567

Contents lists available at ScienceDirect

Journal of Quantitative Spectroscopy & Radiative Transfer

journal homepage: www.elsevier.com/locate/jqsrt

Polarimetric imaging for the detection of synthetic models of SARS-CoV-2: A proof of concept

Emilio Gomez-Gonzalez[a,b,+], Olga Muñoz[c], Juan Carlos Gomez-Martin[c], Jesus Aceituno-Castro[c,d], Beatriz Fernandez-Muñoz[f], Jose Manuel Navas-Garcia[g], Alejandro Barriga-Rivera[a,h,*], Isabel Fernandez-Lizaranzu[a,b], Francisco Javier Munoz-Gonzalez[a], Ruben Parrilla-Giraldez[e], Desiree Requena-Lancharro[a], Pedro Gil-Gamboa[a], José Luis Ramos[c], Cristina Rosell-Valle[f], Carmen Gomez-Gonzalez[j], Maria Martin-Lopez[f], Maria Isabel Relimpio-Lopez[k,l,m], Manuel A. Perales-Esteve[a,i], Antonio Puppo-Moreno[b,j], Francisco Jose Garcia-Cozar[n,o], Lucia Olvera-Collantes[n,o], Silvia de los Santos-Trigo[p], Emilia Gomez[q], Rosario Sanchez-Pernaute[f], Javier Padillo-Ruiz[b], Javier Marquez-Rivas[a,b,r]

[a] Group of Interdisciplinary Physics, Department of Applied Physics III at the ETSI Engineering School, Universidad de Sevilla, Seville 41092, Spain
[b] Institute of Biomedicine of Seville, Spain
[c] Cosmic Dust Laboratory, Instituto de Astrofísica de Andalucía, CSIC, Granada 18008, Spain
[d] Centro Astronomico Hispano Alemán, Almeria 04550, Spain
[e] Technology and Innovation Centre, Universidad de Sevilla, Sevilla 41012, Spain
[f] Unidad de Producción y Reprogramación Celular, Red Andaluza de Diseño y Traslación de Terapias Avanzadas, Fundacion Publica Andaluza Progreso y Salud, Sevilla 41092, Spain
[g] EOD-CBRN Group, Spanish National Police, Sevilla 41011, Spain
[h] School of Biomedical Engineering, The University of Sydney, NSW 2006, Australia
[i] Department of Electronic Engineering at the ETSI Engineering School, Universidad de Sevilla, Seville 41092, Spain
[j] Service of Intensive Care, University Hospital 'Virgen del Rocio', Sevilla 41013, Spain
[k] Department of General Surgery, College of Medicine, Universidad de Sevilla, Seville 41009, Spain
[l] Department of Ophthalmology, University Hospital 'Virgen Macarena', Sevilla 41009, Spain
[m] OftaRed, Institute of Health 'Carlos III', Madrid 28029, Spain
[n] Department of Biomedicine, Biotechnology and Public Health, University of Cadiz, Cadiz 11003, Spain
[o] Instituto de Investigación e Innovación Biomedica de Cádiz (INIBICA), Cadiz 11009, Spain
[p] Corporación Tecnológica de Andalucía, Sevilla 41092, Spain
[q] Joint Research Centre, European Commission, Sevilla 41092, Spain
[r] Service of Neurosurgery, University Hospital 'Virgen del Rocío', Sevilla 41013, Spain

ARTICLE INFO

Article history:
Received 11 July 2022
Revised 4 March 2023
Accepted 4 March 2023
Available online 6 March 2023

Keywords:
COVID-19
Mueller polarimetry
Polarimetric imaging
SARS-CoV-2
Virus detection

ABSTRACT

Objective: To conduct a proof-of-concept study of the detection of two synthetic models of severe acute respiratory syndrome coronavirus 2 (SARS-CoV-2) using polarimetric imaging.
Approach: Two SARS-CoV-2 models were prepared as engineered lentiviruses pseudotyped with the G protein of the vesicular stomatitis virus, and with the characteristic Spike protein of SARS-CoV-2. Samples were prepared in two biofluids (saline solution and artificial saliva), in four concentrations, and deposited as 5-μL droplets on a supporting plate. The angles of maximal degree of linear polarization (DLP) of light diffusely scattered from dry residues were determined using Mueller polarimetry from87 samples at 405 nm and 514 nm. A polarimetric camera was used for imaging several samples under 380–420 nm illumination at angles similar to those of maximal DLP. Per-pixel image analysis included quantification and combination of polarization feature descriptors in 475 samples.

* Corresponding author.
E-mail address: abrivera@us.es (A. Barriga-Rivera).
+ Deceased author (21st January 2023).

https://doi.org/10.1016/j.jqsrt.2023.108567
0022-4073/© 2023 The Author(s). Published by Elsevier Ltd. This is an open access article under the CC BY-NC-ND license (http://creativecommons.org/licenses/by-nc-nd/4.0/)

Main results: The angles (from sample surface) of maximal DLP were 3° for 405 nm and 6° for 514 nm. Similar viral particles that differed only in the characteristic spike protein of the SARS-CoV-2, their corresponding negative controls, fluids, and the sample holder were discerned at 10-degree and 15-degree configurations.

Significance: Polarimetric imaging in the visible spectrum may help improve fast, non-contact detection and identification of viral particles, and/or other microbes such as tuberculosis, in multiple dry fluid samples simultaneously, particularly when combined with other imaging modalities. Further analysis including realistic concentrations of real SARS-CoV-2 viral particles in relevant human fluids is required. Polarimetric imaging under visible light may contribute to a fast, cost-effective screening of SARS-CoV-2 and other pathogens when combined with other imaging modalities.

© 2023 The Author(s). Published by Elsevier Ltd.
This is an open access article under the CC BY-NC-ND license
(http://creativecommons.org/licenses/by-nc-nd/4.0/)

1. Introduction

The wide spread of coronavirus disease 2019, known as COVID-19, has mobilized unprecedented economic resources for the quest of finding new ways of fighting the propagation of infectious diseases. A vast amount of strategies have been implemented from almost all fields of research, including molecular biology [1,2], pharmacology [3–5], genetics [6,7], medical imaging [8–11], and artificial intelligence [12] among others, with varying levels of success [13]. Three main lines of action can be highlighted: prevention [14], treatment [15], and detection (both for screening and diagnostic purposes) [16]. Severe social distancing measures have been imposed worldwide to reduce the propagation of the so-called severe acute respiratory coronavirus 2 (SARS-CoV-2). With the arrival of a collection of vaccines [17,18], some of these measures have been eased in those territories with high vaccination rates [19–22]. However, an important surge in the number of new infections was reported following a period after inoculation of the first vaccines [23,24]. In addition, population that have not had full access to preventive medication is still large. Therefore, the need for testing and monitoring for the spread of the SARS-CoV-2 remains in some territories.

A family of molecular testing devices have recently emerged to identify past [25,26] and on-going infections [25,27]. While debate still continues about the establishment of a gold standard technique for the diagnosis of COVID-19, polymerase chain reaction (PCR) remains as the accepted benchmark. However, rapid tests have enabled screening at the point of care within minutes [28], although with reduced accuracy.

Optical techniques are being also explored for the detection of a variety of pathogens. They range from the detection of the Zika virus in mosquitoes fed with infected human blood using infrared spectroscopy [29] to the detection of hepatitis B and C viruses [30] and Dengue [31] in human samples using Raman and fluorescence spectroscopy. Most recent efforts aim to detect SARS-CoV-2 models [32] and the SARS-CoV-2 virus [33–36].

These techniques are opening new possibilities for rapid concurrent mass screening of contagious diseases and have the potential to re-shape the screening approaches currently in place at transport hubs such international airports. However, the optical information contained in biological samples has not been fully exploited. For example, Mueller polarimetry [37,38], a technique employed to characterize the photo-polarimetric characteristics of the sample , can be used for the detection and discrimination of biological structures [39–41]. In fact, Mueller polarimetry is used in astrobiology, in the search for biological molecules (biosignatures) outside the Earth [42–44]. Recent works highlight the potential of the analysis of the vectorial properties of light beams interacting with samples for many biomedical applications [45], including the detection of viruses [46,47]. However, further studies in this field are required to clarify whether said detection and discrimination in complex biological media (e.g., blood) relate to specific elements (e.g., viruses), or to the effects that they produce in tissues or structures. These approaches range from physics-based methods to artificial intelligence (e.g., machine learning) algorithms. Notably, computational simulations show the potential of the evaluation of changes of circular polarization under ultraviolet light to detect and discern viral model particles with the characteristic Spike protein of the SARS-CoV-2 [48].

Here we have examined the use of polarimetric imaging under visible light for the rapid identification of engineered viral particles (two laboratory models of the SARS-CoV-2, with and without its Spike protein) deposited as fluid preparations on surfaces in an experimental proof-of-concept study. Firstly, we use the Cosmic Dust Laboratory (CODULAB) instrument [49] for obtaining the Mueller matrix of the light reflected by the surfaces of interest as a function of the viewing angle θ (Fig. 1). This first set of measurements spans a broad range of angles. Thus, they provide the optimal observing geometry for polarimetric imaging. Secondly, based on the previous results, we designed a polarimetric imaging set-up (Fig. 2) for simultaneous imaging of several samples placed on a supporting plate. Polarimetric imaging shows potential for detection of elements in compound backgrounds [50] and classification of materials [51], although registered images are difficult to analyze because of the complex nature of physical processes involved and their multiplicative random speckle noise [52]. Recent approaches for their analysis include the use of deep learning techniques [53].

In this work, samples (i.e., droplets) were easily segmented against the background, and a per-pixel image processing methodology was applied. Several quantitative descriptors based on the measured polarimetric features were defined, calculated at the per-pixel level and later integrated at the per-sample level. This is the same procedure employed by the authors for the analysis of hyperspectral images of the same type of samples which allowed for detecting and characterizing those ones with viral content in similar concentrations [32,34].

The use of polarimetry for the detection of respiratory viruses in dried fluids presents many challenging aspects. Among them, their relatively low concentration in the samples and the genetic variability, the presence of optically active biomolecules (e.g., sugars, amino acids, nucleic acids and other chiral elements that can rotate the polarization of light) in different orientations, the inherent variability of human samples - particularly in patients with any pathology- and the effects of the physical process of sample drying under the ambient temperature and humidity on the selected surface for deposition of the fluids (e.g., formation of crystals with similar size than the wavelength of the analysis light).

Consequently, this work presents an initial report based on an empirical approach. We designed a well-controlled experiment to

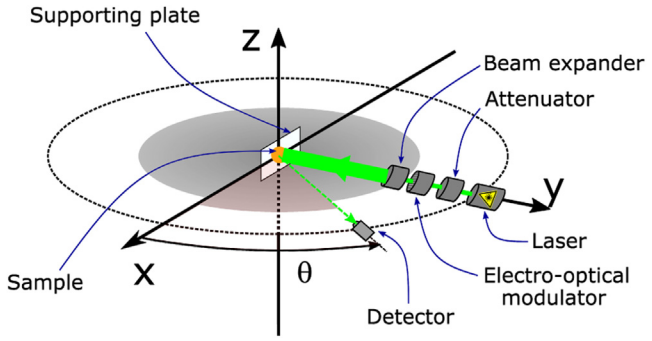

Fig. 1. Schematic of the optical setup used to determine the viewing angle (θ) that maximizes the degree of linear polarization of the diffusely reflected light. A continuous-wave laser illuminated the sample. The light beam passed through an optical attenuator to reduce its intensity, and an electro-optical modulator modified its polarization state. A beam expander provided homogenous illumination of the sample.

minimize the aforementioned factors under standardized experimental conditions: i) viral particles here were engineered in the laboratory to reduce the genetic variability that appears in natural infections, ii) the fluids used to re-suspend the viral preparations were chosen to mimic physiological conditions, and iii) following previous works [32,34], the volume of each fluid droplet was 5-uL, and the diameter of the resulting dried residue was 5 mm approximately.

The employed viral models were lentiviral particles (LP), commonly used in many biological and medical applications [32,34]. They were pseudotyped with the G protein of the vesicular stomatitis virus (G-LP) and, independently, with the Spike protein of the SARS-CoV-2 (S-LP).

Overall, lentiviral particles are quasi-spherical, with an average diameter of about 100 nm. G-LPs have an approximately 'smooth' outer surface while S-LPs present the protruding, rod-like, SARS-CoV-2 spikes of about 10–20 nm. Images of these viral models can be found in references [54–56]. As detailed later, the illumination in our experiments comprised visible laser (405 nm and 514 nm) sources for the point measurements, and filtered light from a broadband halogen source (380–420 nm) for the polarimetric images.

The aim in this work was to determine, under these very well controlled conditions, whether a polarimetric analysis could benefit a new strategy for the detection of viruses based on the analysis of images of dry fluid droplets.

We have followed a strategy for empirical analyses, in increasing order of complexity. Hence, we have studied three types of samples: i) pure (synthetic) fluids, of two types (saline solution and artificial saliva), ii) fluids with non-transfected culture medium of the viruses, and iii) fluids with the culture medium and the viruses (of two types).

The positive samples (i.e., those with viruses), and the corresponding negative controls (i.e., those without viruses but with the culture medium) were prepared in the same four concentrations. These values were selected following the methodology of previous papers [32,34] using similar samples (fluids and engineered viruses), with the same general goal (i.e., the detection of SARS-CoV-2). Samples of pure fluids were also, obviously, negative.

2. Materials and methods

We analyze fluid samples containing two different types of synthetic models of the SARS-CoV-2, namely, lentiviral particles pseudotyped with the G protein of the vesicular stomatitis virus (G-LP), and with the characteristic Spike (S) protein of the SARS-CoV-2 (S-LP). Both models are ribonucleic acid viruses of similar size and shape as the SARS-CoV-2, also having a double lipid capsid, but different in the presence of the Spike protein on their surface. Samples were prepared in two different types of biofluids, a phosphate buffered solution (PBS), i.e., a type of saline solution, and artificial saliva (AS), much more similar to natural saliva. In each fluid, four levels of concentration (i.e., viral load) were tested. Negative controls included solutions of viral culture media (without viruses) in the same concentrations and pure fluids. We use fluid droplets with a volume of 5 uL, deposited (by pipetting) on the supporting surface. This volume is larger than those of 'respiratory droplets' commonly referred in airborne transmission of respiratory diseases.

Optical set-ups in this study include: i) The CODULAB instrument, to measure the reflection Mueller matrix of dry samples deposited on a supporting plate as function of the reflection angle (θ_R) or its complementary the so-called viewing angle ($\theta = 90° - \theta_R$) using as light sources two visible wavelength diode lasers (Fig. 1), and ii) a specific polarimetric imaging configuration under band-pass filtered halogen illumination (Fig. 2). Numerical descriptors of polarimetric features were then computed and combined in a per-pixel image processing procedure.

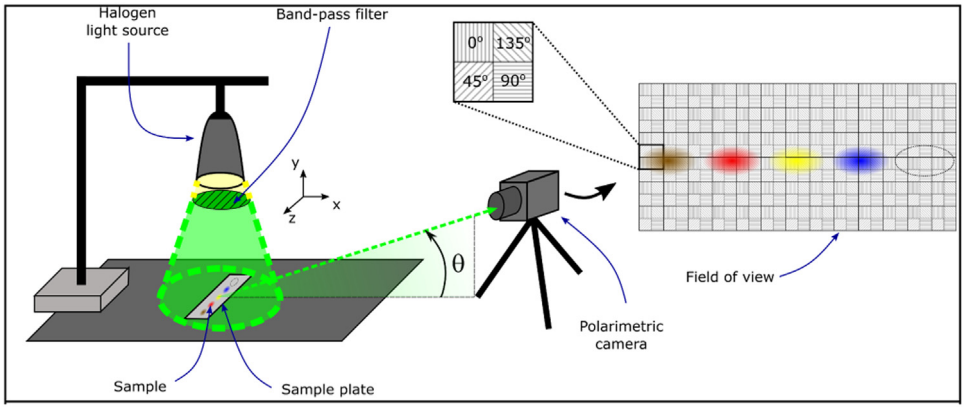

Fig. 2. Schematic of the setup used for polarimetric imaging. Samples were deposited as a row of four fluid droplets onto a supporting plate. They contained preparations of VSV-G pseudotyped lentiviral particles (brown area), SARS-CoV-2 Spike pseudotyped lentiviral particles (red area) and the corresponding culture medium (negative control, in the same concentration, yellow area) and the pure fluid (blue area). In addition, an equivalent region of the plate (dotted ellipse) was defined as background. The samples were illuminated with a halogen light source with a band-pass filter between 380 nm and 420 nm. The polarimetric camera was placed at a working distance of 90 mm from the sample, with the viewing axis in $\theta = 10°$ and $\theta = 15°$ configurations. Raw images were later demosaiced into independent I0, I90, I45 and I135 images (corresponding to each registered direction of linear polarization) for further processing.

2.1. Lentiviral particles pseudotyped with the G protein of the vesicular stomatitis virus (G-LP)

Lentiviral particles pseudotyped with protein G of the vesicular stomatitis virus (VSV) were produced as described in a previous publication [32]. Briefly, human embryonic kidney (HEK) 293 cells were transfected with lentiviral plasmids encoding ZsGreen, the viral envelope VSV-G protein, and the Tat, Gag-Pol and Rev genes. These cells were then cultured in Gibco Dulbecco's Modified Eagle Medium (DMEM) and incubated during 48 h at 37 °C and 5% CO_2. The culture medium was supplemented with 10% bovine serum (Biowest, Nuaillé, France), and the antibiotics penicillin (100 UI·mL^{-1}) and streptomycin (100 µg·mL^{-1}) (Millipore-Sigma, Missouri, USA) were added to prevent bacterial infections. Lentiviral particles were precipitated using Lenti-X reagent (Takara Bio Inc, Shiga, Japan). Following centrifugation, the supernatant was removed and the concentrate was frozen at −80 °C.

2.2. Lentiviral particles pseudotyped with the spike protein of the SARS-CoV-2 (S-LP)

Similarly, lentiviral particles were pseudotyped with the Spike protein of the SARS-CoV-2 as described in another publication [34]. These engineered viral particles exhibit the molecular structure of the SARS-CoV-2 capsid characterized by the protuberant Spike protein that appears inserted on the surface of the virions. The preparation methodology was similar to that described above. Note that in this case, HEK 293 cells were transfected with a plasmid encoding the SARS-CoV-2 spike protein instead [57]. The preparation was cultured, precipitated and stocked as described previously for the VSV-G pseudotyped lentiviral particles.

2.3. Controls

Negative control samples were prepared following the same methodology described for pseudotyping lentiviral particles without transfecting the HEK cells, that is, the cells were cultured without adding plasmids and, therefore without viral particles. Incubation, precipitation and stocking was performed as described above. Resuspension of the media thus prepared was carried out to achieve the same titer as for the viral preparations in both media, PBS and AS. In addition, PBS and AS alone were also used as controls.

2.4. Sample preparation

On the day of the experiment, an aliquot was defrosted to prepare an initial stock with a titer of $20{\cdot}10^3$ transducing units (TU)·µL^{-1}. The aliquot was re-suspended in two different media: Dulbecco's phosphate buffered saline (reference D8537, Millipore-Sigma, Missouri, USA) and stabilized artificial saliva for medical and dental research (reference 1700–0305, Pickering Laboratories, California, USA [58]). These standardized products allow for the reproducibility of the experiments of the presented proof-of-concept research. Serial dilutions were then prepared to achieve a final concentration of 4000 TU·µL^{-1}, 3000 TU·µL^{-1}, 1500 TU·µL^{-1} and 800 TU·µL^{-1}. As detailed in a previous paper [32], this lowest value corresponds approximately to $8{\cdot}10^8$ copies·mL^{-1}, i.e., the viral load of potential 'super-spreaders' of COVID-19. Note that non-transfected samples were prepared in the same way to generate the controls. A total of 467 fluid droplets were prepared (87 for point polarimetry and 380 for imaging polarimetry).

2.5. Point mueller polarimetry

CODULAB [49,59] was designed to measure the full scattering Mueller matrix of clouds of cosmic dust analogues and atmospheric aerosols as function of the scattering angle. Here CODULAB was adapted to measure the reflection Mueller matrix, **R**, as function of the viewing angle, θ, of dry samples deposited on a supporting plate. The surfaces were illuminated with diode lasers emitting 10 mW at $\lambda = 405$ nm or $\lambda = 514$ nm orthogonally to the supporting plate (Fig. 1). Electro-optic modulation of the incident beam combined with lock-in detection enabled concurrent determination of the elements $R_{ij}(\theta, \lambda)$ of the 4×4 reflection matrix, $\mathbf{R}(\theta, \lambda)$. The modulated laser beam is reflected by the residue located on the supporting plate, which is mounted on a x-y rotating table to control the illumination geometry. To ensure homogenous illumination over the entire dry-residue, a 5–10x zoom Galilean beam expander with magnification set to 7x was positioned between the modulator and the sample. Assuming homogeneous illumination on a 5 mm-diameter disk, the corresponding irradiance on the samples was about 509 W·m^{-2}. The reflected light was collected by a photomultiplier tube detector (9828A Electron tubes). This detector moves along a 1-m diameter ring in steps of 1 or 5° spanning the viewing angle range from 0° to −70°, with a blind region between 83° and −87°. The detector was located 62 cm away from the surface under study. For each data point at a given reflexion angle, 1000 measurements were conducted in about 1 s. Therefore, one single data point was the average of 1000 measurements. The error of one data point was the standard deviation of the series of 1000 measurements. A diaphragm was located at the detector to control solid angle subtended by the detector window. Therefore, each data point can be considered as an average value of the full dry residue. These measurements are labelled as "point measurements" throughout the paper.

Initially, we investigated if any of the $R_{ij}(\theta, 405\text{ nm})$ elements could help with discriminating clean surfaces from those covered with usual surface contaminants i.e., home dust and (artificial) saliva. A wide variety of surface materials (polymethyl methacrylate, polytetrafluoroethylene, steel, aluminum, cardboard) was tested. Different orientations of the sample holder relative to the incident laser light were also tested. The optimal illumination geometry was found with the laser light incident perpendicular to the supporting plate. Subsequently, we tested if the $-R_{21}(\theta, \lambda)/R_{11}(\theta, \lambda)$ curve at 405 nm and 514 nm could discriminate samples with viral particles from their negative controls. The $-R_{21}(\theta, \lambda)/R_{11}(\theta, \lambda)$ ratio is, for unpolarized incident light, equal to the degree of linear polarization, hereafter DLP [49]. In this set of measurements, the samples were placed on a polytetrafluoroethylene (PTFE) sheet (BSH, Seville, Spain), 1 mm in thickness, and approximately 22 mm × 22 mm of surface.

For each fluid, preparation, and concentration, a 5-µL droplet was deposited onto a holder plate. Upon complete evaporation of the water content only dry residues remained, and the sample plate was positioned vertically. A total of 87 fluid droplets were analyzed with this set-up (Table 1). They included 16 samples of G-LP in PBS, 16 samples of S-LP in PBS and 8 samples of S-LP in artificial saliva at four different concentrations, their corresponding negative controls, and droplets of pure fluid. Measurements were carried out in a dark room with average temperature of 22 °C and humidity of 55%.

2.6. Polarimetric imaging

Based on the results obtained as described in section E, we developed a polarimetric imaging setup. In this case, the supporting plate was placed on a Vibraplane 5602–3672–31 imaging table (Kinetic Systems, Phoe nix, USA). The samples were illuminated with a XD-301 halogen light source (Alltion, Guangxi, China), placed 35 mm above the center of the sample plate. A FKB-VIS-40 band-pass filter (Thorlabs, New Jersey, USA) with central wavelength 400 nm was used to allow light with wave-

Table 1
Number of samples used for Point Mueller polarimetry.

Sample type	Concentrations							
	C1		C2		C3		C4	
	P	N	P	N	P	N	P	N
G-LP in PBS	4	4	4	4	4	4	4	4
S-LP in PBS	4	4	4	4	4	4	4	4
S-LP in AS	2	1	2	1	2	1	2	1
AS	11							
BG	5							

Table 1. Distribution of the 92 samples (87 fluid droplets and 5 droplet-equivalent background areas) used for point Mueller polarimetry. Concentrations were C1 = 800 TU·μL^{-1}, C2 = 1500 TU·μL^{-1}, C3 = 3000 TU·μL^{-1} and C4 = 4000 TU·μL^{-1}. G-LP = Lentiviral particles pseudotyped with the G protein of the vesicular stomatitis virus. S-LP = Lentiviral particles pseudotyped with the spike protein of the SARS-CoV-2. *P* = positive sample (solution with viral particles and culture medium), *N*= negative sample (solution with culture medium). PBS = phosphate buffered solution, AS = artificial saliva, BG = background (supporting plate).

Table 2
Number of samples used for imaging polarimetry at θ=10°.

Sample type	Concentrations							
	C1		C2		C3		C4	
	P	N	P	N	P	N	P	N
G-LP in PBS	4	4	4	4	4	4	4	4
S-LP in PBS	4		4		4		4	
G-LP in AS	4	4	4	4	4	4	4	4
S-LP in AS	4		4		4		4	
PBS	16							
AS	16							
BG	32							

Table 2. Distribution of the 160 samples (128 fluid droplets and 32 droplet-equivalent background areas) used for imaging polarimetry at 10°. Concentrations were C1 = 800 TU·μL^{-1}, C2 = 1500 TU·μL^{-1}, C3 = 3000 TU·μL^{-1} and C4 = 4000 TU·μL^{-1}. G-LP = Lentiviral particles pseudotyped with the G protein of the vesicular stomatitis virus. S-LP = Lentiviral particles pseudotyped with the spike protein of the SARS-CoV-2. *P* = positive sample (solution with viral particles and culture medium), *N*= negative sample (solution with culture medium). PBS = phosphate buffered solution, AS = artificial saliva, BG = background (supporting plate).

Table 3
Number of samples used for imaging polarimetry at θ=15°

Sample type	Concentrations							
	C1		C2		C3		C4	
	P	N	P	N	P	N	P	N
G-LP in PBS	8	8	8	8	8	8	8	8
S-LP in PBS	8		8		8		8	
G-LP in AS	8	8	8	8	7	7	8	8
S-LP in AS	8		8		7		8	
PBS	32							
AS	31							
BG	63							

Table 3. Distribution of the 315 samples (252 fluid droplets and 63 droplet-equivalent background areas) used for imaging polarimetry at 15°. Concentrations were C1 = 800 TU·μL^{-1}, C2 = 1500 TU·μL^{-1}, C3 = 3000 TU·μL^{-1} and C4 = 4000 TU·μL^{-1}. G-LP = Lentiviral particles pseudotyped with the G protein of the vesicular stomatitis virus. S-LP = Lentiviral particles pseudotyped with the spike protein of the SARS-CoV-2. *P* = positive sample (solution with viral particles and culture medium), *N*= negative sample (solution with culture medium). PBS = phosphate buffered solution, AS = artificial saliva, BG = background (supporting plate).

lengths comprised between 380 nm and 420 nm. A TRI050S-PC polarimetric camera (Lucid Vision Labs, Richmond, Canada) with a VS-LDA20 lens with focal length of 20 mm and maximum aperture of f/2.1 (Vital Vision, Paya Lebar, Singapore) was placed at a working distance of 90 mm from the sample supporting plate, and with the viewing axis forming a certain angle θ (of 10° and 15°) with the plate surface, as illustrated in Fig. 2. The camera has a sensor with a total of 2448 × 2048 pixels arranged in units of four individual pixels, each one having a linearly polarized filter to register the intensities corresponding to polarization directions of 0°, 45°, 90° and 135° (as depicted in Fig. 2). Each of those units (of four polarized pixels) therefore defines an 'effective pixel' at the corresponding location in the image plane defined by the field of view of the camera . The values of irradiance registered at each direction of polarization at the location of each effective pixel were further combined -after demosaicing raw sensor file- the into four independents 1224 × 1024 pixel images (denoted as I_0, I_{90}, I_{45} and I_{135}). Values of irradiance are further expressed normalized in 8 bits per pixel. The experiment was conducted in a dark room at ~24 °C and 50% relative humidity.

Polarization information was obtained from dry residues of each preparation. In doing so, 5-μL droplets were placed on a PTFE plate, also 1 mm in thickness, and approximately 50 mm × 20 mm of surface, with a spacing of about 8 mm to reduce potential crosstalk between the light registered by neigbouring pixels of the imaging sensor. Each imaging preparation contained one droplet of each specimen for each type of dissolving fluid, that is, a total of four droplets in a row corresponding to G-LP, S-LP, control (viral culture medium), and pure fluid. An additional space was left in the row for delineating an empty region of the supporting plate equivalent (in image pixels) to a droplet, identified as background (BG). The fluid droplets were left to dry for at least 20 min.

The total number of samples analysed by imaging polarimetry was 475, corresponding to 380 fluid droplets and 95 equivalent areas of background. Table 2 details the number of samples (160 fluid droplets and BG areas) employed for 10-degree imaging and Table 3 those (315 fluid droplets and BG areas) for 15-degree imaging. The average number of pixels per fluid droplet and their corresponding standard deviation were 358±124 pixels for 10-degree imaging and 1281±581 pixels for 15-degree experiments. An additional set of 28 samples (with 200 pixels per droplet) was employed to evaluate the distribution of the illumination over the field of view of the camera.

As described in a previous paper [34], a simplified disk model of a droplet imaged by a camera with an optical axis perpendicular to the plate yields an approximately equivalent pixel volume of 14 nL at 10° and 4 nL at 15°.

2.7. Polarimetric imaging data analysis

The Stokes vector S_r of the light reflected by the sample in a given direction was obtained as described in Eq. (1) from the light intensity registered by the detector. As indicated, I_0, I_{90}, I_{45} and I_{135} denote the light intensity (irradiance) at the detector with the optical axis of the polarizers (analysers) set to 0, 90, 45 and 135°, respectively. Fig. 2 shows the distribution of polarizer filters at each pixel of the camera sensor. Note also linearly polarized light was registered only, and therefore, s_3 was not determined in this analysis.

$$S_r = \begin{bmatrix} s_0 \\ s_1 \\ s_2 \\ s_3 \end{bmatrix} = \begin{bmatrix} I_0 + I_{90} \\ I_0 - I_{90} \\ I_{45} + I_{135} \\ - \end{bmatrix} \quad (1)$$

The DLP together with the angle of linear polarization (ALP) of the reflected beam are defined as functions of the Stokes parameters as in Eq. (2) and Eq. (2) respectively:

$$DLP = \frac{\sqrt{s_1^2 + s_2^2}}{s_0} \quad (2)$$

$$ALP = \frac{1}{2}\arctan\left(\frac{s_2}{s_1}\right) \tag{3}$$

For the analysis of the polarimetric images, we defined normalized Stokes parameters as described in Eq. (4), where max(s_0) denotes the maximum value of s_0 in the polarimetric image.

$$S_{r,n} = \begin{bmatrix} s_{0n} \\ s_{1n} \\ s_{2n} \\ s_{3n} \end{bmatrix} = \begin{bmatrix} s_0/\max(s_0) \\ s_1/s_0 \\ s_2/s_0 \\ - \end{bmatrix} \tag{4}$$

Note that s_{3n} is not determined in the employed set-up. In addition, we included three parameters, defined as relative differences between any combination of the Stokes parameters, as described in Eqs. (5-7).

$$A_1 = \frac{s_1 - s_0}{s_1 + s_0} \tag{5}$$

$$A_2 = \frac{s_2 - s_0}{s_2 + s_0} \tag{6}$$

$$A_3 = \frac{s_1 - s_2}{s_1 + s_2} \tag{7}$$

Using an in-house computer program for polarimetric image analysis developed in Matlab® R2020b (The Mathworks Inc., Massachusetts, USA), droplet images were segmented. As indicated, each imaged plate contained four dry droplets (corresponding to G-LP in fluid, S-LP in fluid, control (viral culture medium) in fluid, and the pure fluid) and the additional background area. The corresponding values of the registered intensities for each direction of polarization (I_0, I_{45}, I_{90}, and I_{135}) and the 'polarimetric features' (namely, DLP, ALP, s_{0n}, s_{1n}, s_{2n}, A_1, A_2, and A_3) at each pixel were determined and stored.

2.8. Statistical analysis

Mean values of the DLP and ALP at each reflection angle (point measurements) were graphed for each type of viral particle and fluid, their corresponding negative controls and pure fluids, and the supporting plate. Droplet-averaged values of DLP, ALP, s_{0n}, s_{1n}, s_{2n}, A_1, A_2, and A_3 were calculated from the corresponding pixels for each sample from the polarimetric images, and their values and uncertainties were represented in boxplots. In addition, several combinations of polarimetric features were represented as two- and three-dimensional plots to explore their ability to discern among the different types of samples.

Normality of value distributions was discarded using the Chi-squared test. The two-tailed Wilcoxon rank-sum test was performed on the arithmetic combinations of the parameters to distinguish the different samples under examination. Statistical significance was considered at the 95% confidence level. P-values below 0.0001 were considered as zero. Errors were reported here as the standard deviation.

2.9. Ethics and data availability

The study was approved by the Regional Research and Ethics Committee of University Hospitals 'Virgen Macarena and Virgen del Rocío', Seville, Spain (reference 0945-N-20, approved on 4/21/2020). Data supporting this work are available from the authors under reasonable request.

3. Results

It is known that biomolecules can alter the state of polarization of the scattered light [45]. In order to explore whether this phenomenon can be exploited for the intended detection and quantification of viruses, we first determined the optimal reflection angle that maximized the DLP of the light reflected by the (dry) fluid samples. Then, the polarimetric images were obtained as close as possible to the optimal viewing angle. A set of numerical features describing the polarization of the light reflected off the samples was numerically calculated for the image pixels corresponding to each sample and analyzed.

3.1. Determination of the angle of maximal DLP

The objective of the point polarimetry experiments was to find the optimal illumination and observing geometry, and the corresponding viewing angle θ (i.e., the complementary of the reflection angle) at which the DLP of the reflected light was maximum, as this allows for maximizing the information obtained from the polarization properties of the sample under examination. Fig. 3A shows the value of the DLP obtained from a preparation of S-LP in artificial saliva at the highest concentration and its negative control (i.e., samples with fluid and culture medium but without viral particles).

As shown in Fig. 3, all measured DLP curves show their maximum values at small viewing angles. In all cases, from their maximum values, the DLP curves decreased as the viewing angle increased. As presented in Fig. 3A, there were statistically significant differences between the measured maximum value of the DLP for the S-LP samples and their corresponding negative controls.

Similar results were obtained at 514 nm, as displayed in Fig. 3, panel B. The value of the DLP showed statistically significant differences (*p-value*=0.00) among the viral concentrations. These differences were larger at lower viewing angles. Also note that, at this wavelength, the sample plate exhibits a peak at 6°, as shown in Fig. 3B.

3.2. Viral detection using polarimetric imaging

To obtain redundant information simultaneously from many points of a given sample preparation we used a polarimetric camera placed to image the samples at a certain angle. However, the viewing direction of the camera must balance two opposing factors: the small value of maximal DLP determined by point polarimetry (with respect to the supporting plate), which would define an approximately tangential imaging acquisition, and the need to obtain 'large enough' images of the sample droplets to provide a sufficient number of pixels per droplet for numerical assessment. When the camera is close to the plane defined by the sample supporting plate, the distortion and parallax of the imaged field of view increase notably. Besides the geometric distortion of perspective, it must be considered that the sample volumes corresponding to each image pixel also differ.

Images were therefore obtained at $\theta = 10°$ and 15°, as shown in Fig. 5 and Fig. 6, respectively. Note these angles do not maximize the value of DLP as described previously for 405 nm. However, considering that the light source was band-pass filtered between 380 nm and 420 nm, and that the (center) axis of illumination was perpendicular to the sample supporting plate, these observation angles provided sufficient information about the vectorial properties of the scattered light. As mentioned in the methodology, the Stokes parameters s_0, s_1 and s_2 were obtained from the light intensities captures by the camera in the different linear polarization angles. Next, the DLP and the ALP were computed. Images built by calculating all these parameters, pixel by pixel, are displayed in Fig. 5 and Fig. 6. The values of the normalized Stokes parameter s_{2n} and the newly defined relative difference A_3 are shown in Fig. 7 for both, the 10° and 15° viewing angles.

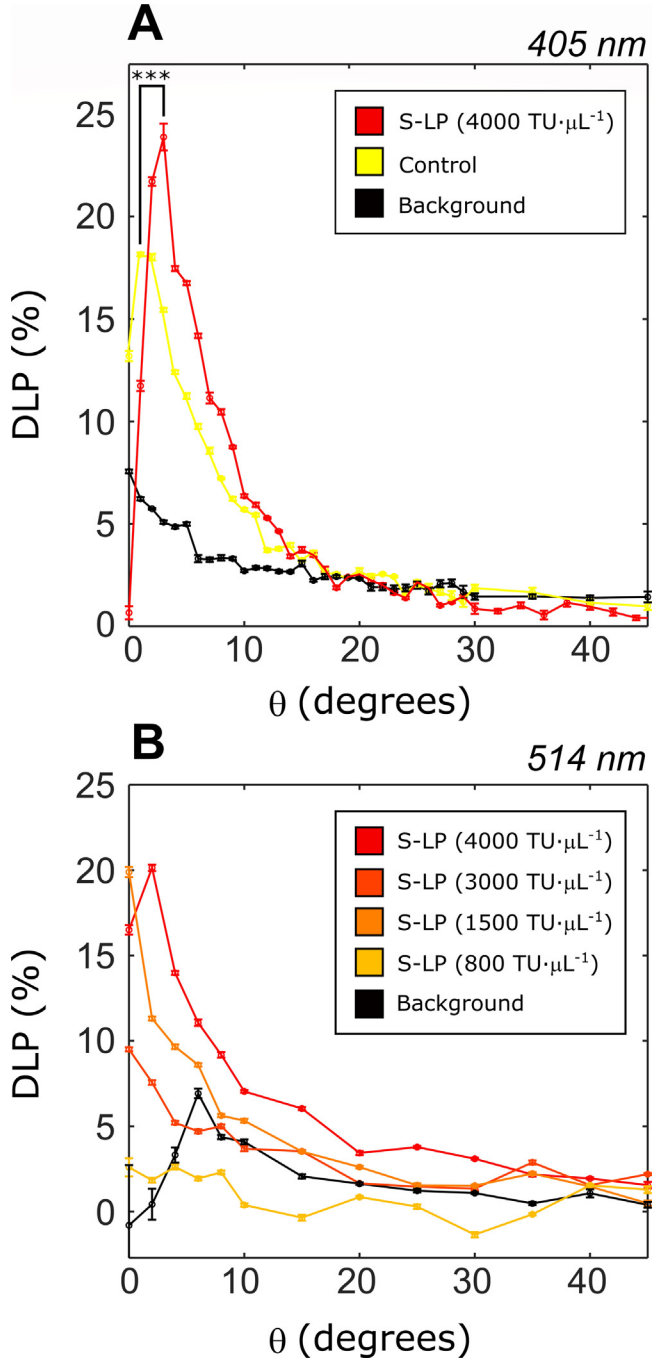

Fig. 3. Measured DLP curves as functions of the viewing angle (θ) at 405 nm (Panel A) and 514 nm (Panel B) of dry residues of preparations in artificial saliva of lentiviral particles pseudotyped with the S protein of the SARS-CoV-2 (S-LP) and the corresponding negative controls. Each data point (solid symbols) shows the average value of 1000 measurements obtained in 1 second. The error bars denote the standard deviation. The background represents the DLP obtained from the supporting (clean) PTFE plate. ***p-value < 0.0001 from two-tailed Wilcoxon rank-sum test.

3.3. Analysis of the illumination

As indicated (and depicted in Fig. 2), the wide field illumination required for simultaneous imaging of multiple droplets was achieved using a conical beam setup and, therefore, the distribution of illumination along the transversal axis of the camera field of view (line of the droplets, z-axis in Fig. 2) was uneven. To evaluate this effect, test exams were performed with droplets of artificial saliva without any addition (i.e., with identical, pure fluid samples). Test droplets were deposited in four equispaced positions along the transversal axis of the field of view of the camera (Fig. 2). The values of irradiance received by the camera sensor in the four directions of polarization (I_0, I_{45}, I_{90}, and I_{135}) were registered, and the normalized Stokes parameters (s_{0n}, s_{1n} and s_{2n}) and the relative differences defined (A_1, A_2 and A_3) were calculated. Box plots were obtained, the Chi-squared normality test was performed, and the corresponding set of values were compared. As shown in Fig. 4, the normalized Stokes parameters s_{1n} and s_{2n} and their relative difference A_3 were independent of their positions along the droplet row. The positions of G-LP, S-LP, AS and BG samples in Fig. 7 corresponded, approximately, to positions P1, P2, P3 and P4 of test droplets in Fig. 4.

4. Discussion

The spread of the SARS-CoV-2 virus has been an obvious cause of severe concern worldwide. Despite the high vaccination rates achieved in many territories, the transmission of new variants of the virus is raising fears, as these strains incorporate mutations in the spike protein able to reduce the affinity of existing antibodies [60,61]. Therefore, continued mass testing of the population remains as one of the principal measures of public health to contain the spread of the pathogen. Along these lines, numerous molecular technologies have been developed for the detection of the genetic material of the virus [62], viral antigens [63], or the specific immune response triggered after the infection [64]. In addition, optical technologies also boost SARS-CoV-2 detection capabilities by providing new methods able to identify the presence of the virus [35,65]. Recent works include the analysis of hyperspectral images of diffuse reflectance for the detection and quantification of synthetic viral models [32] and of SARS-CoV-2 in human samples [34], as reported by the authors.

It is important to note that image-based virus detection schemes allow for rapid analysis of multiple samples (all droplets included within the field of view of the imaging system), using a reagent-free, relatively simple and safe (non-contact) configuration suitable for use by minimally trained operators, even in resource-constrained settings. The results reported here on the differentiation between fluid samples containing two similar viral models of SARS-CoV-2 using polarimetric imaging analysis can be incorporated along with other existing technologies for making optical detection more robust.

We first explored whether there were differences between the DLP of the light reflected by samples containing one type of viral particles comparable to the SARS-CoV-2 virus (i.e., S-LP) and their negative controls. Certainly, the differences found were more evident at higher concentrations. Note that the liquid samples were left to dry, and therefore, these differences were caused by the composition of the residues, in this case, the presence or not of lentiviral particles. Therefore, samples with S-LPs in different concentrations were successfully differentiated using repeated DLP point measurements of the reflected light at a certain angle range at two wavelengths. This result converges with the aforementioned detection and quantification of the same type of samples, in the same biofluids and concentrations (both as liquid droplets and dry residues) using hyperspectral image analysis [34]. On the other hand, it is important to note that differences in the drying conditions of biofluids may alter the Mueller matrix elements as functions of the viewing angle. In particular, drying conditions (surface material, temperature, humidity, *etc.*) may determine the crystallization patterns of inorganic salts [66,67]. In this work, droplets were left to dry under approximately the same experimental conditions. However, local differences in the formation of crystals and other dry residues are likely to appear in the sample. These differ-

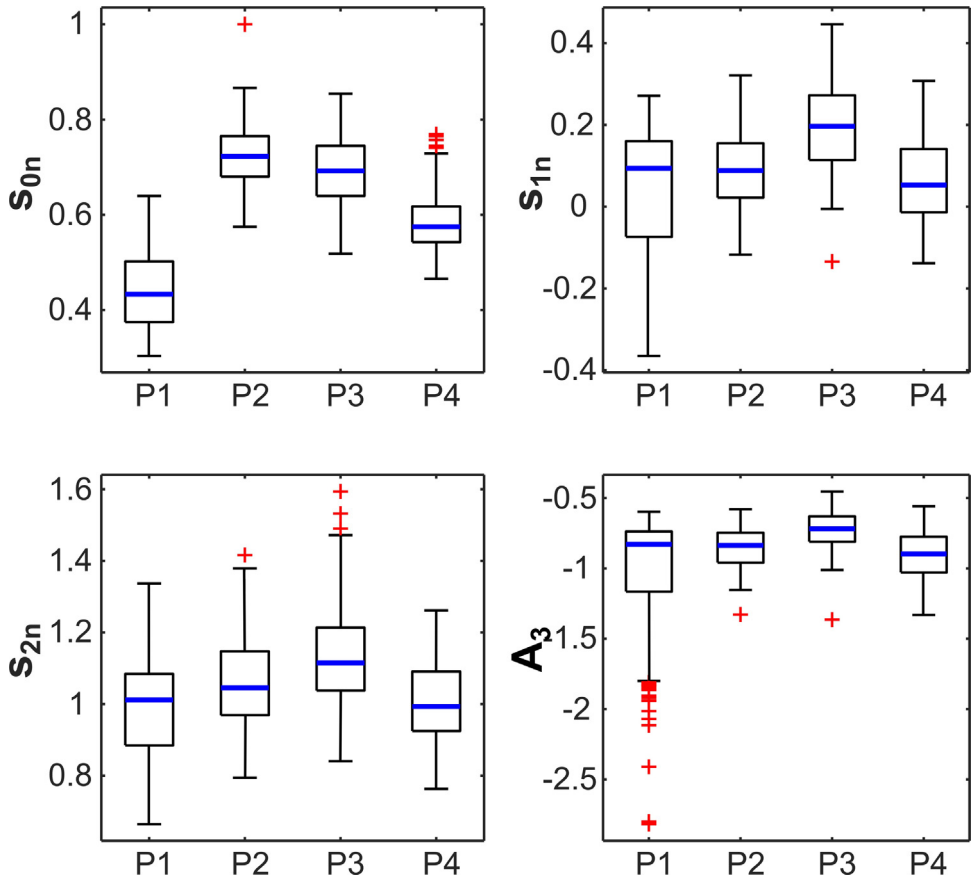

Fig. 4. Box plots of the normalized Stokes parameters (s_{0n}, s_{1n} and s_{2n}) and the relative difference A_3 for droplets of artificial saliva (without any addition) placed in four equispaced positions (P) along the axis of the imaged field of view (z-axis of Fig. 2). The parameters s_{2n} and A_3 (later used in Fig. 7) cannot be distinguished based on their position along the sample row (p<0.05).

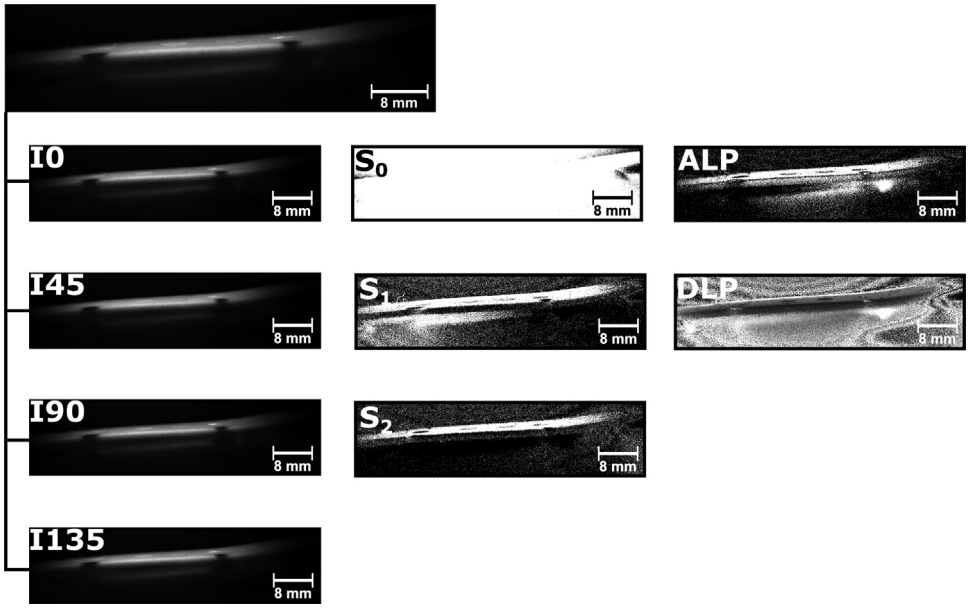

Fig. 5. Polarimetric images obtained with the camera placed in a 10-degree configuration (viewing angle) in artificial saliva. Top image is the luminance image of the sample. The four (dry) fluid droplets correspond (from left to right) to G-LP, S-LP, control, and pure fluid. Images I0, I45, I90 and I135 were obtained after demosaicing and correspond to irradiance of the 0-degree, 45-degree, 90-degree and 135-degree polarization components. Images s_0, s_1 and s_2 were obtained by computing the Stokes parameters at each pixel. Likewise, images corresponding to the angle and degree of linear polarization (ALP and DLP) were computed.

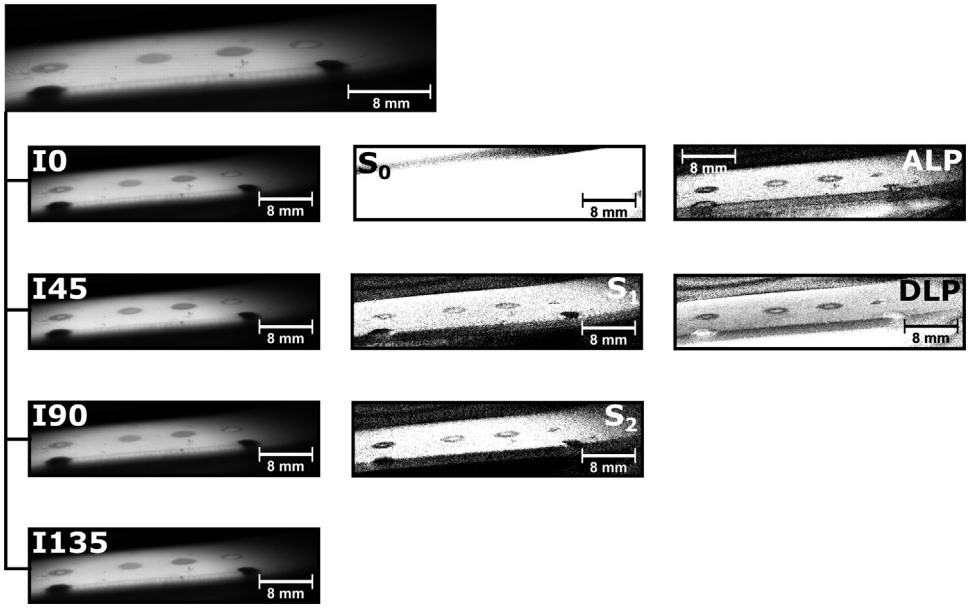

Fig. 6. Polarimetric images obtained with the camera placed in a 15-degree configuration (viewing angle). Top image is the luminance image of the samples in artificial saliva. The four (dry) fluid droplets correspond (from left to right) to G-LP, S-LP, control, and pure fluid. Images I0, I45, I90 and I135 were obtained after demosaicing and correspond to irradiance of the 0-degree, 45-degree, 90-degree and 135-degree polarization components. Images s_0, s_1 and s_2 were obtained by computing the Stokes parameters at each pixel. Likewise, images corresponding to the angle and degree of linear polarization (ALP and DLP) were computed.

ences and the overall impact of the drying conditions remains to be studied.

The next step was to compare among samples with the two similar viral particles, G-LP and S-LP, being the minimal difference among them the presence of the characteristic spike protein of the SARS-CoV-2. For that purpose, we developed the described polarimetric imaging set-up with θ within the range previously determined from the point measurements. This imaging approach also possesses several limitations: (1) uneven illumination over the whole sample as a consequence of using conical illumination, (2) a relatively wide bandwidth of the light source, (3) crosstalk from reflected light at different sample points, (4) differences in the illumination angles caused by the rugosity of the supporting plate, (5) image distortion and aberrations produced by the lens of the camera, or (6) parallax distortion due to the small imaging angle among others. However, the advantages of the proposed methodology overcome some of these limitations, as imaging allows for the simultaneous acquisition of information from many samples (i.e., suitable for mass testing implementations) and from many points (pixels) of each sample (i.e., providing data suitable for enhanced extraction of information). In addition, we propose the combined use of multiple parameters for a precise numerical analysis of the differences in the state of polarization of the scattered light which are expected to allow for effective discernment of different virions in the samples (and their absence in the corresponding negative controls). Unlike other applications of polarimetric imaging, each sample here was characterized by an extended set of parameters that quantify, directly or indirectly, vectorial properties of the diffusedly reflected light. Those parameters include the commonly used irradiances at each direction of the analyzer optical axis (I_0, I_{90}, I_{45} and I_{135}), the (original and normalized) Stokes parameters (s_o, s_1, s_2, s_{on}, s_{1n}, s_{2n}), and their derived magnitudes (DLP, ALP) plus the newly introduced relative differences (A_1, A_2 and A_3).

As shown in Fig. 4A, the uneven illumination in the polarimetric imaging setup described here (due to the conical source) had a non-negligible effect on the spatial distribution of the values of the normalized Stokes parameter s_{0n}. Note however that the parameters s_{1n} and s_{2n}, and their relative difference A_3, did not exhibit said dependence with the position along the axis of the samples (z-axis in Fig. 2, values for pure artificial saliva in Fig. 4). Therefore, differences found in the values of these parameters in positive and negative samples (Fig. 7) can be mainly attributed to their composition, and not to their relative position along (the axis of) the holder. These results could possibly be improved by using a collimated illumination beam.

Furthermore, as indicated, the proposed imaging approach simplifies the experimental setup and reduces the level of training required to perform a test. Unfortunately, to exploit the information contained in the polarization state of the scattered light, a low imaging angle is required. While differences in the polarization properties of the light could be maximized at the 5° imaging configuration, the reduced dimensions of the resulting sample images prevent from obtaining redundant information from larger groups of pixels. Note that, as shown in Fig. 7, even though samples with G-LPs and S-LPs could be distinguished at a 10-degree configuration, differentiation from the negative control was not possible using one parameter alone. Nevertheless, differentiation among the two viral species and the negative control was successful using a 15° imaging configuration. This can be explained in terms of substantially lower sample areas covered by each pixel in the image. In addition, in said imaging configuration, the fluid medium (AS) and the supporting background material (PTFE) produced similar changes in the polarization parameters under study that hampered the differentiation between these two samples. Therefore, the alterations of the polarization state of the incident light produced by the biological content were sufficient for differentiating dried fluid samples containing two similar viral particles, one expressing the G protein of the VSV, and the other, the S protein of the SARS-CoV-2, both within the same lentiviral system.

As presented here, these differences can be enhanced if several parameters are combined and processed using multivariate analysis. Note that our technique obtains an overall estimation over a relatively large area. Experiments here were conducted in two different setups: i) for point measurements (with a device designed for characterizing astronomical dust), a beam expander was used to illuminate the whole area of the sample, and ii) for polarimetric imaging (using a camera), estimators were obtained by averaging the values of a large group of pixels (within the same droplet,

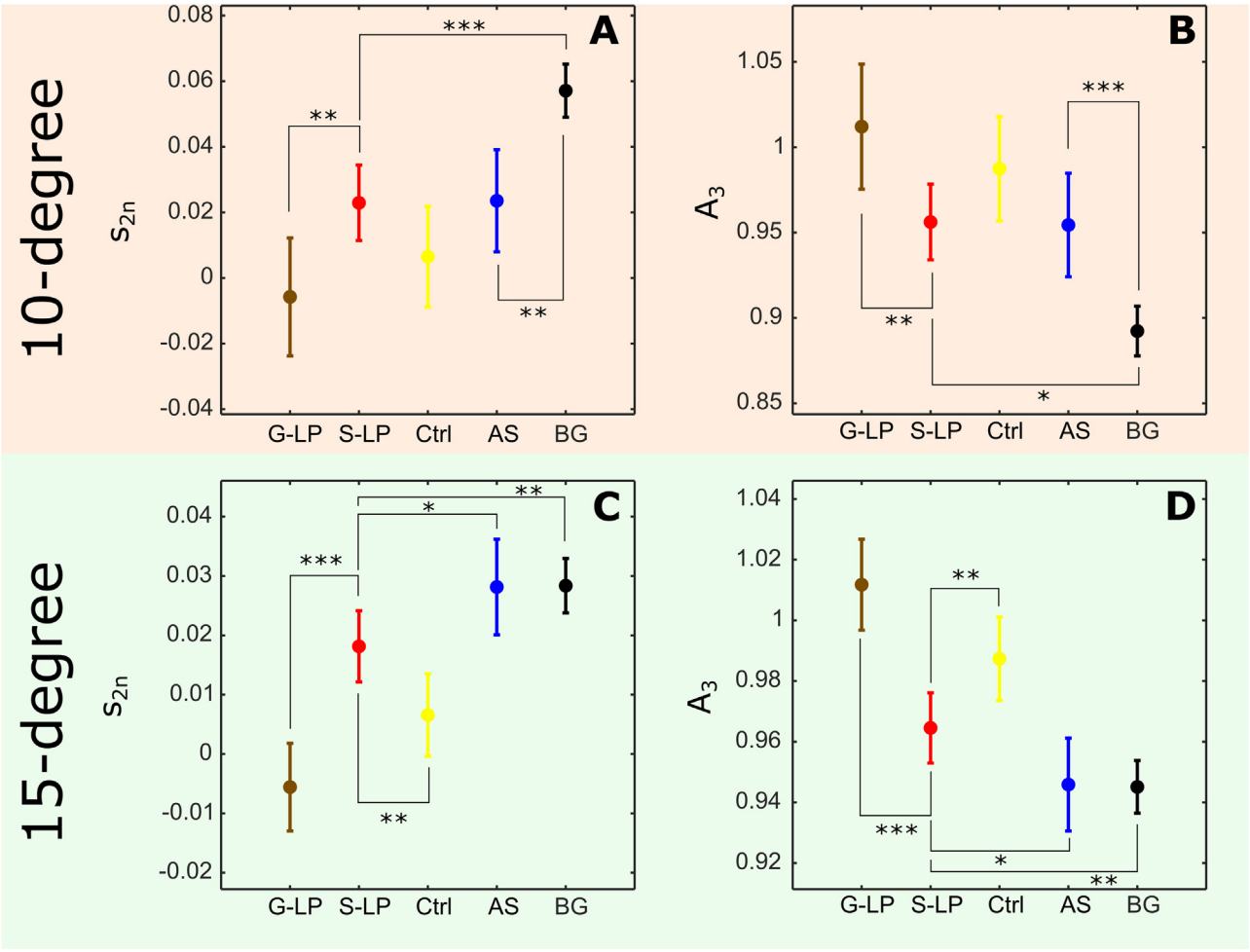

Fig. 7. Polarimetric parameters. Panels **A** and **B** show the mean values of the s_{2n} and A_3 parameters respectively obtained with the polarimetric camera in a 10° configuration. Panels **C** and **D** show the mean values of the s_{2n} and A_3 parameters respectively obtained with the polarimetric camera in a 15° configuration. Error bars denote the calculated uncertainties. *p-value<0.1, **p-value<0.05, ***p-value < 0.005 from *t*-test ($n = 4$). These parameters were obtained from samples containing lentiviral particles pseudotyped with the G protein of the vesicular stomatitis virus (G-LP) and lentiviral particles pseudotyped with the spike protein of the SARS-CoV-2 (S-LP) prepared at 4000 TU·μL^{-1} concentration. Negative controls (Ctrl) were obtained from non-transfected culture media in the same concentrations. All biological specimens were re-suspended in artificial saliva (AS). The background (BG) given by the supporting plate was also characterized.

after segmentation of pixels which may present inhomogeneities or imaging artifacts). Therefore, polarimetric values obtained here account for a spatially averaged of the contribution of the viral particles contained within each sample; random effects were therefore cancelled out in this approach.

Although there is an evident need for extending the results presented herein beyond the use of laboratory engineered viruses in synthetic biofluids, we anticipate that the biological signature of viral pathogens, that is, the molecular composition that allows for their detection, embeds certain 'information' in the reflected light. Note, for example, that previous studies on imaging spectroscopy [32,34] found important characteristic features at similar wavelengths. Notably, the results obtained here are aligned with the aforementioned numerical simulations [48] in which changes in the circular polarization of ultraviolet light (310 nm) allowed for the discernment of computational viral models similar to the ones employed in our experiments.

In this work we explored the use of this technology for identifying potentially contaminated surfaces containing dry residues of the engineered viral models. A supporting plate containing dry samples was used as a model of a fomite. Although a deep study of said limits of detection has not been addressed here, it is possible to provide an estimate of the volume fraction of viral particles distinguishable with this technique. On the one hand, if the overall diameter of the synthetic viral particles used here is assumed to be approximately 100 nm, the volume of a virion would be approximately 10^{-15} cm^3. Given the highest concentration of the viral preparations was 4000 TU·μL^{-1}, and assuming that only 0.1% of the viral particles of the preparations were infective [32], this concentration can be expressed, in physical units, as $4{\cdot}10^9$ copies·mL^{-1}. Therefore, the volume fraction of viral particles in a droplet was approximately $4{\cdot}10^{-6}$. Assuming the volume fraction of the solids in the biofluids to be approximately 0.005, the volume ratio of virions in dry droplets is approximately $2{\cdot}10^{-4}$. On the other hand, a similar rational can be followed to determine the volume fraction of SARS-CoV-2 viral particles in human samples. Using data from Wylie et al. [68], said volume fraction ranges from 10^{-9} to 10^{-3}. Therefore, this approach alone has limited potential, as it can only target the upper tier. However, it can be combined with other imaging technologies for the detection of viruses such as hyperspectral imaging [32,34]. These type of approaches could be exploited for mass screening of respiratory diseases, including COVID-19. In doing so, studies that include human specimens should be conducted to determine the sensitivity and specificity of polarimetric imaging, and its limits of detection, by itself and combined with other imaging modalities (e.g., hyperspectral). As mentioned before, human salivary and respiratory secretions are complex mixtures of a wide variety of biological molecules, and their

composition may change from person to person, and from time to time. For example, one should expect important differences in the composition of these secretions between morning time, after a whole night fasting, and minutes after a meal. The experiments presented in this study were designed to avoid these variations. Thus, the only differences in the composition of the synthetic biofluids relate to the presence of the two types of viral particles, under controlled laboratory conditions (e.g., drying). After having shown significant differences in the polarimetric measurements obtained here, the next step would be to test this in a more realistic scenario.

If properly linked to other approaches, optical detection of pathogens by a reagent-free, non-contact, easy-to-implement approach has the potential to provide truly useful tools to face biosecurity hazards, as it would allow for scanning of multiple samples within very short time frames, opening its use to transport hubs or mass events.

5. Conclusions

In summary, we present a proof-of-concept study on the use of polarimetric image analysis for detection and discernment of synthetic models of SARS-CoV-2 in dry fluid droplets under visible light. Experiments were conducted using two types of engineered viral models (lentiviral particles with and without the Spike protein), in two fluids (saline solution and artificial saliva), in four concentrations. Mueller polarimetry of 120 samples determined the optimal angles for polarimetric imaging. Changes in the linear polarization of light diffusely scattered by other 475 samples were quantified in a per-pixel approach.

Polarimetric imaging shows potential to improve fast, non-contact detection and identification of viral particles in multiple dry fluid samples simultaneously, particularly as combined with other (e.g., hyperspectral) imaging modalities and extensive computational analysis. Additional physical and mathematical descriptors may be obtained to better characterize, optically and numerically, samples containing viruses. Further studies with human fluid samples -especially, fresh saliva- are required, as this approach might contribute to cost-effective, relatively easy-to-implement virus screening including SARS-CoV-2.

Author statement

Conceptualization: EGG, OM, JAC

Methodology: EGG, OM, JMNG, JCGM, JAC, BFM, JMR, ABR, FJGC, EG, RSP, MIRL, APM, JPR, SST

Investigation: All authors.

Software: IFL, FJMG, RPG, DLR, PGG, ABR, EGG, JMNG, OM, JCGM, JLR

Data curation: OM, JCGM, JLR, IFL, FJMG, RPG, DLR, PGG, ABR, JMNG, EGG, BFM, CRV, MML, FJGC, LOC, RSP,

Data analysis: All authors.

Biological samples: BFM, FJGC, CRV, MML, LOC, RSP, APM, CGG, JMR

Mueller polarimetry: OM, JCGM, JLR, EGG, JMNG

Polarimetric imaging: EGG, JMNG, IFL, FJMG, RPG, DLR, PGG, ABR, MAPE, JMR

Visualization, figures: ABR, EGG, JMNG, JMR

Writing, draft preparation, and editing: EGG, ABR, OM, JCGM, JMNG, JMR, BFM, FJGC

Declaration of Competing Interest

Emilio Gomez-Gonzalez reports financial support was provided by Spanish Ministry of Science and Innovation, Institute of Health 'Carlos III'. Emilio Gomez-Gonzalez reports financial support was provided by Spanish Ministry of Science and Innovation and ERDF. Francisco Jose Garcia-Cozar reports financial support was provided by Spanish Ministry of Science and Innovation, Institute of Health 'Carlos III'. Alejandro Barriga-Rivera reports financial support was provided by Spanish Ministry of Science and Innovation and ERDF. Olga Muñoz reports financial support was provided by Center of Excellence 'Severo Ochoa'. Juan Carlos Gomez-Martin reports financial support was provided by Center of Excellence 'Severo Ochoa'. Jose Luis Ramos reports financial support was provided by Center of Excellence 'Severo Ochoa'. Olga Muñoz reports financial support was provided by Spanish Ministry of Science and Innovation (LEONIDAS Grant). Juan Carlos Gomez-Martin reports financial support was provided by Spanish Ministry of Science and Innovation (LEONIDAS Grant). Jose Luis Ramos reports financial support was provided by Spanish Ministry of Science and Innovation (LEONIDAS Grant). Emilio Gomez-Gonzalez has patent Apparatus and method for the optical detection of pathogens at a distance pending to Universidad de Sevilla and Andalusian Health Service. Alejandro Barriga-Rivera has patent Apparatus and method for the optical detection of pathogens at a distance pending to Universidad de Sevilla and Andalusian Health Service. Javier Marquez-Rivas has patent Apparatus and method for the optical detection of pathogens at a distance pending to Universidad de Sevilla and Andalusian Health Service. One coauthor serves as Handling Associate Editor for the Journal of Quantitative Spectroscopy & Radiative Transfer - Olga Muñoz

Data Availability

Data will be made available on request.

Acknowledgements

This study was funded by grants number COV20–00080 and COV20–00173 of the 2020 Emergency Call for Research Projects about the SARS-CoV-2 virus and the COVID-19 disease of the Institute of Health 'Carlos III', Spanish Ministry of Science and Innovation, and by grant number EQC2019–006240-P funded by MICIN/AEI/10.13039/501100011033 and by "ERDF A way of making Europe". ABR was supported by grant number RTI2018–094465-J-I00 funded by MICIN/AEI/10.13039/501100011033 and by "ERDF A way of making Europe". The work of OM, JCGM, and JLR has been partially funded by grant LEONIDAS (RTI2018–095330-B-100), and the Center of Excellence Severo Ochoa award to the Instituto de Astrofísica de Andalucía (SEV-2017–0709). This work has been supported by the European Commission through the Joint Research Center (JRC) HUMAINT project.

The authors would like to gratefully acknowledge the assistance of the members of the Explosive Ordnance Disposal – Chemical, Biological, Radiological & Nuclear (EOD-CBRN) Group of the Spanish National Police, whose identities cannot be disclosed, and who are represented here by JMNG.

The authors would like to express their special gratitude to Emilio Gomez-Gonzalez, who sadly passed away in January 2023, and whose wisdom and willingness have been key in the development of this work and many other projects.

Supplementary materials

Supplementary material associated with this article can be found, in the online version, at doi:10.1016/j.jqsrt.2023.108567.

References

[1] Das A, Ahmed R, Akhtar S, Begum K, Banu S. An overview of basic molecular biology of SARS-CoV-2 and current COVID-19 prevention strategies. Gene Rep 2021;101122.

[2] Kaul D. An overview of coronaviruses including the SARS-2 coronavirus—molecular biology, epidemiology and clinical implications. Curr Med Res Practice 2020;10(2):54–64.
[3] Huang L, et al. Progress in the research and development of anti-COVID-19 drugs. Front Public Health 2020;8:365.
[4] Little P. Non-steroidal anti-inflammatory drugs and covid-19. British Medical Journal Publishing Group; 2020. ed:.
[5] Belete TM. Review on up-to-date status of candidate vaccines for COVID-19 disease. Infect Drug Resist 2021;14:151.
[6] John G, et al. Next-generation sequencing (NGS) in COVID-19: a tool for SARS-CoV-2 diagnosis, monitoring new strains and phylodynamic modeling in molecular epidemiology. Curr Issues Mol Biol 2021;43(2):845–67.
[7] Starr TN, et al. Prospective mapping of viral mutations that escape antibodies used to treat COVID-19. Science 2021;371(6531):850–4.
[8] Suri J, et al. Systematic review of artificial intelligence in acute respiratory distress syndrome for COVID-19 lung patients: a biomedical imaging perspective. IEEE J Biomed Health Inform 2021.
[9] Wehbe RM, et al. DeepCOVID-XR: an artificial intelligence algorithm to detect COVID-19 on chest radiographs trained and tested on a large US clinical data set. Radiology 2021;299(1):E167–76.
[10] Desai SB, Pareek A, Lungren MP. Deep learning and its role in COVID-19 medical imaging. Intelligence-Based Med 2020;3:100013.
[11] Ng M-Y, et al. Imaging profile of the COVID-19 infection: radiologic findings and literature review. Radiology 2020;2(1):e200034.
[12] Gunasekeran DV, Tseng RMWW, Tham Y-C, Wong TY. Applications of digital health for public health responses to COVID-19: a systematic scoping review of artificial intelligence, telehealth and related technologies. NPJ Digital Med 2021;4(1):1–6.
[13] Heaven WD. Hundreds of AI tools have been built to catch covid. None of them helped. MIT Technol Rev 2021.
[14] GÜNER HR, Hasanoğlu İ, Aktaş F. COVID-19: prevention and control measures in community. Turk J Med Sci 2020;50(SI–1):571–7.
[15] Cascella M, Rajnik M, Aleem A, Dulebohn S, Di Napoli R. Features, evaluation, and treatment of coronavirus (COVID-19). StatPearls 2022.
[16] Yüce M, Filiztekin E, Özkaya KG. COVID-19 diagnosis—A review of current methods. Biosens Bioelectron 2021;172:112752.
[17] Creech CB, Walker SC, Samuels RJ. SARS-CoV-2 vaccines. JAMA 2021;325(13):1318–20.
[18] Hodgson SH, Mansatta K, Mallett G, Harris V, Emary KR, Pollard AJ. What defines an efficacious COVID-19 vaccine? A review of the challenges assessing the clinical efficacy of vaccines against SARS-CoV-2. Lancet Infect Dis 2021;21(2):e26–35.
[19] Leung K, Wu JT, Leung GM. Effects of adjusting public health, travel, and social measures during the roll-out of COVID-19 vaccination: a modelling study. Lancet Public Health 2021;6(9):e674–82.
[20] Bauer S, et al. Relaxing restrictions at the pace of vaccination increases freedom and guards against further COVID-19 waves. PLoS Comput Biol 2021;17(9):e1009288.
[21] Burki TK. Lifting of COVID-19 restrictions in the UK and the Delta variant. Lancet Respiratory Med 2021;9(8):e85.
[22] Han E, et al. Lessons learnt from easing COVID-19 restrictions: an analysis of countries and regions in Asia Pacific and Europe. Lancet North Am Ed 2020.
[23] Lanzavecchia S, Beyer KJ, Bolo SEvina. Vaccination is not enough: understanding the increase in cases of COVID-19 in Chile despite a high vaccination rate. Epidemiologia 2021;2(3):377–90.
[24] Keehner J, et al. Resurgence of SARS-CoV-2 infection in a highly vaccinated health system workforce. N Engl J Med 2021;385(14):1330–2.
[25] Deeks JJ, et al. Antibody tests for identification of current and past infection with SARS-CoV-2. Cochrane Database Syst Rev 2020(6).
[26] Hoffman T, et al. Evaluation of a COVID-19 IgM and IgG rapid test; an efficient tool for assessment of past exposure to SARS-CoV-2. Infect Ecol Epidemiol 2020;10(1):1754538.
[27] Yamayoshi S, et al. Comparison of rapid antigen tests for COVID-19. Viruses 2020;12(12):1420.
[28] Song Q, et al. Point-of-care testing detection methods for COVID-19. Lab Chip 2021;21(9):1634–60.
[29] Fernandes JN, et al. Rapid, noninvasive detection of Zika virus in Aedes aegypti mosquitoes by near-infrared spectroscopy. Sci Adv 2018;4(5):eaat0496.
[30] Anwar S, Firdous S. Optical diagnostic of hepatitis B (HBV) and C (HCV) from human blood serum using Raman spectroscopy. Laser Phys Lett 2015;12(7):076001.
[31] Firdous S, Anwar S. Optical diagnostic of dengue virus infected human blood using raman, polarimetric and fluorescence spectroscopy. Dengue 2017:75.
[32] Gomez-Gonzalez E, et al. Hyperspectral image processing for the identification and quantification of lentiviral particles in fluid samples. Sci Rep 2021;11:16201.
[33] Kitane DL, et al. A simple and fast spectroscopy-based technique for Covid-19 diagnosis. Sci Rep 2021;11:16740.
[34] Gomez-Gonzalez E, et al. Optical imaging spectroscopy for rapid, primary screening of SARS-CoV-2: a proof of concept. Sci Rep 2022;12:2356.
[35] Lukose J, Chidangil S, George SD. Optical technologies for the detection of viruses like COVID-19: progress and prospects. Biosens Bioelectron 2021:113004.
[36] Maddali H, Miles CE, Kohn J, O'Carroll DM. Optical biosensors for virus detection: prospects for SARS-CoV-2/COVID-19. ChemBioChem 2021;22(7):1176.
[37] Anderson R. Measurement of Mueller matrices. Appl Opt 1992;31(1):11–13.
[38] Chipman RA, Sornsin EA, Pezzaniti JL. Mueller matrix imaging polarimetry: an overview. In: Proceedings of the International Symposium on Polarization Analysis and Applications to Device Technology, 2873; 1996. p. 5–12. International Society for Optics and Photonics.
[39] Mazumder N, Qiu J, Kao F-J, Diaspro A. Mueller matrix signature in advanced fluorescence microscopy imaging. J Opt 2017;19(2):025301.
[40] Badieyan S, et al. Detection and discrimination of bacterial colonies with Mueller matrix imaging. Sci Rep 2018;8(1):1–10.
[41] Schucht P, et al. Visualization of white matter fiber tracts of brain tissue sections with wide-field imaging Mueller polarimetry. IEEE Trans Med Imaging 2020;39(12):4376–82.
[42] Kothari N, Jafarpour A, Trebino R, Thaler TL, Bommarius AS. Astrobiological polarimeter. Astrobiology 2008;8(6):1061–9.
[43] Wang B, Sparks WB, Germer TA, Leadbetter A. A spectroscopic polarimeter for detecting chiral signatures in astrobiological samples. In: Proceedings of the Instruments and Methods for Astrobiology and Planetary Missions XII, 7441; 2009. International Society for Optics and Photonics.
[44] Martin WE, et al. Polarized optical scattering signatures from biological materials. J Quant Spectrosc Radiat Transfer 2010;111(16):2444–59.
[45] He C, He H, Chang J, Chen B, Ma H, Booth MJ. Polarisation optics for biomedical and clinical applications: a review. Light: Sci Appl 2021;10(1):1–20.
[46] Le H-M, Le TH, Phan QH. Mueller matrix imaging polarimetry technique for dengue fever detection. Opt Commun 2022;502:127420.
[47] Guo B, et al. Detection of virus particles by scattering field using the multiperspective polarization modulation imaging method. JOSA B 2021;38(12):3592–600.
[48] Ashraf MW, Ranjan R, Diaspro A. Circular intensity differential scattering of light to characterize the coronavirus particles. JOSA B 2021;38(5):1702–9.
[49] Muñoz O, et al. Experimental phase function and degree of linear polarization curves of millimeter-sized cosmic dust analogs. Astrophysical J Supplement Series 2020;247(1):19.
[50] Xie F, Chen J. A demosaicing algorithm based on local directional gradients for polarization image. In: Proceedings of the 2021 International Conference on Computing, Networking, Telecommunications & Engineering Sciences Applications (CoNTESA); 2021. p. 40–4. IEEE.
[51] Krishna TVT, Creusere CD, Voelz DG. Passive polarimetric imagery-based material classification robust to illumination source position and viewpoint. IEEE Trans Image Process 2010;20(1):288–92.
[52] Ayed IB, Mitiche A, Belhadj Z. Polarimetric image segmentation via maximum–likelihood approximation and efficient multiphase level-sets. IEEE Trans Pattern Anal Mach Intell 2006;28(9):1493–500.
[53] D. Xiao, Z. Wang, Y. Wu, X. Gao, and X. Sun. "Terrain Segmentation in Polarimetric SAR Images Using Dual-Attention Fusion Network". IEEE Geosci Remote Sens Lett, 19, pp. 1–5, 2022.
[54] Desmaris N N, Bosch A, Salaün C, et al. Production and neurotropism of lentivirus vectors pseudotyped with Lyssavirus envelope glycoproteins. Mol Ther 2001;4(2):149–56.
[55] Uhlig KM, Schülke S, Scheuplein VAM, et al. Lentiviral protein transfer vectors are an efficient vaccine platform and induce a strong antigen-specific cytotoxic T cell response. J Virol 2015;89:9044–60.
[56] Lu M, Uchil PD, Li W, et al. Real-time conformational dynamics of SARS-CoV-2 spikes on virus particles. Cell Host Microbe 2020;28(6):880–91.
[57] Crawford KH, et al. Protocol and reagents for pseudotyping lentiviral particles with SARS-CoV-2 spike protein for neutralization assays. Viruses 2020;12(5):513.
[58] Pickering Laboratories. "1700-0305 Artificial Saliva Safety Data Sheet," 2015.
[59] Muñoz O, et al. Experimental determination of scattering matrices of dust particles at visible wavelengths: the IAA light scattering apparatus. J Quant Spectrosc Radiat Transfer 2010;111(1):187–96.
[60] Kannan SR, Spratt AN, Sharma K, Chand HS, Byrareddy SN, Singh K. Omicron SARS-CoV-2 variant: unique features and their impact on pre-existing antibodies. J Autoimmun 2022;126:102779.
[61] Oude Munnink BB, et al. The next phase of SARS-CoV-2 surveillance: real-time molecular epidemiology. Nat Med 2021;27:1518–24.
[62] Patchsung M, et al. Clinical validation of a Cas13-based assay for the detection of SARS-CoV-2 RNA. Nature Biomed Eng 2020;4(12):1140–9.
[63] Mak GC, et al. Evaluation of rapid antigen test for detection of SARS-CoV-2 virus. J Clin Virol 2020;129:104500.
[64] Paiva KJ, et al. Validation and performance comparison of three SARS-CoV-2 antibody assays. J Med Virol 2021;93(2):916–23.
[65] G. Vargas "A review of recent reports on the applications of optical technologies to detect SARS-CoV-2," Proc. SPIE 11633, Design and Quality for Biomedical Technologies XIV, 1163305, 2021.
[66] Bel'skaya LV, Sarf EA, Solonenko AP. Morphology of dried drop patterns of saliva from a healthy individual depending on the dynamics of its surface tension. Surfaces 2019;2(2):395–414.
[67] Yakhno TA, et al. Drops of biological fluids drying on a hard substrate: variation of the morphology, weight, temperature, and mechanical properties. Tech Phys 2010;55:929–35.
[68] A.L. Wyllie, et al. "Saliva or nasopharyngeal swab specimens for detection of SARS-CoV-2". N Engl J Med vol. 383, no 13, p. 1283–6, 2020.